HF-Induced Modulation and Electron Temperature Effects in PMSE: VHF Spectral Diagnostics and Dusty Plasma Interpretation

A. Mahmoudian¹, M. Vazifehkhah¹, M.J. Kosch^{2,3,4}, E. Varberg⁵

5	¹ Institute of Geophysics, University of Tehran, Iran.
6	² Department of Physics, Lancaster University, Lancaster, UK.
7	³ South African National Space Agency (SANSA), Hermanus, South Africa
8	⁴ Dept. of Physics and Astronomy, University of the Western Cape, Bellville, South Africa
9	⁵ EISCAT Scientific Association, Ramfjordmoen, Norway

Corresponding author: Dr. Alireza Mahmoudian, a.mahmoudian@ut.ac.ir

Abstract

10

27

42

43

44

45

46

47

48

49

50

51

52

53

55

56

57

58

59

This study presents the first experimental investigation of Polar Mesospheric Summer 11 Echoes (PMSE) response to high-frequency (HF) pump power modulation using the EIS-12 CAT VHF radar system. Two modulation schemes were employed during a recent cam-13 paign: stepped-power modulation (24 July 2019) and quasi-continuous power sweeping 14 (26 July 2019). Coherent VHF radar spectra were analyzed to evaluate the impact of 15 HF heating on PMSE characteristics. Results consistently show a contraction in the VHF 16 spectral area with increasing HF pump power (40-80 kW), indicating suppression of small-17 scale electron density irregularities. This spectral narrowing is attributed to enhanced 18 diffusion and dust charging processes driven by elevated electron temperatures. The ra-19 tio of diffusion to charging timescales $(\tau_{\rm diff}/\tau_{\rm chg})$ is used as a key diagnostic to interpret 20 these changes. Numerical simulations incorporating realistic dust cloud parameters re-21 produce the observed trends and reveal layer-specific responses, with lower PMSE lay-22 ers exhibiting stronger overshoots and higher dust densities. These findings demonstrate 23 that the spectral area under the VHF echo serves as a sensitive proxy for electron tem-24 perature enhancements during HF heating, offering a valuable diagnostic tool for study-25 ing mesospheric turbulence and dusty plasma dynamics. 26

1 Introduction

PMSEs are striking radar reflections that can be detected at altitudes between 80 to 90 28 km during the summer months at higher latitudes. These strong, coherent echoes were first identified in the 1970s, with researchers such as Ecklund and Balsley (1981) and Czechowsky 30 et al. (1979) noting their unusual intensity. It turns out these echoes originate from the 31 mesopause, where the temperature reaches its lowest point during summer at these lat-32 itudes. Over the years, PMSEs have been captured from various sites using radars op-33 erating at frequencies from 50 MHz to 1.3 GHz, as detailed by Cho and Kelley (1993) 34 and Cho and Rottger (1997), among others. Mahmoudian et al. (2022) made a signif-35 icant breakthrough by delivering the first comprehensive volume observations of the PMSE source region using four radars operating at frequencies of 8, 56, 224, and 930 MHz. Their 37 findings demonstrate that the model effectively accounts for the known neutral air tur-38 bulence alongside the influence of heavy dust particles. This combination, referred to as 39 dusty turbulence, plays a crucial role in explaining the radar cross-section observed at these four frequencies. 41

Recent studies have highlighted the significance of PMSEs as natural tracers of mesospheric wind fields over broad spatial scales, making them valuable tools for mapping neutral atmospheric dynamics (Chau et al., 2018). Sommer and Chau (2016) employed radar imaging with the Middle Atmosphere Alomar Radar System (MAARSY) to demonstrate that PMSEs are composed of ~1km-scale patches of isotropic scatterers. These patchy structures effectively trace small-scale atmospheric dynamics and turbulence.

High-frequency (HF) pump radiowaves have been widely used to investigate the modulation of the polar mesospheric summer echo (PMSE) source region by artificially heating the ionospheric plasma. When transmitted into the D-region (typically 80–90 km altitude), HF heating temporarily elevates the electron temperature, which affects the charging of ice particles and modifies electron diffusivity—key mechanisms governing the formation and persistence of PMSEs (Rietveld et al., 1993; Scales, 2004). This modulation often results in a measurable suppression or enhancement of coherent radar echoes, depending on heating parameters and background conditions (Chilson et al., 2000; Havnes et al., 2003). Early experiments at EISCAT using 224 MHz radar demonstrated that PM-SEs weaken rapidly following heater turn-on and often recover shortly after heater turn-off (Belova et al., 2003; Biebricher et al., 2006). The response is strongly tied to electron cooling and recombination timescales, as well as the interaction between dust particles and the modified plasma environment (Mahmoudian et al., 2011, 2020). These studies

highlight the utility of HF modulation as a diagnostic tool for probing mesospheric plasmaneutral-dust interactions.

To date, the EISCAT facility remains unique in combining a high-power HF radio heat-63 ing transmitter with radars operating at appropriate wavelengths for investigating ar-64 tificially modified polar mesospheric summer echoes (PMSE). As a result, most exper-65 imental studies have been limited to the EISCAT VHF (224 MHz) and UHF (930 MHz) 66 radar frequencies (Rishbeth and van Eyken, 1993). Nonetheless, unmodulated PMSEs have been detected at lower frequencies, such as 2.78 MHz, using colocated instruments (Bremer et al., 1996). Recent developments—including the use of the MORRO radar at 56 MHz (La Hoz and Havnes, 2008; Pinedo et al., 2014; Havnes et al., 2015) and enhance-70 ments to the EISCAT HF facility enabling both heating and radar operations—have made 71 routine observations at longer wavelengths feasible. 72

Considering the model prediction of the different behavior of PMSE at the HF band (e.g., 8 MHz) and VHF (e.g., 224 MHz), a simultaneous experiment using the two radars was conducted at EISCAT in 2013 for the first time (Senior et al., 2014). The diffusion and electron attachment onto the dust particles (dust charging) are the two processes that control the electron density fluctuation amplitude and the corresponding radar echoes (Scales and Mahmoudian, 2016). Mahmoudian and Scales (2013) investigated how radar echoes change over time during PMSE modulation experiments involving positive dust particles. Their findings indicate that the anti-correlation between ion and electron fluctuations is less pronounced before the radiowave is turned off. This occurs due to a slower ambipolar diffusion and a smaller amplitude of ion irregularities, leading to a predicted reduction in the overshoot observed after the turn-off in the presence of positive dust particles. Gunnarsdottir et al. (2023) explored how high-frequency heating affects PMSEs under conditions of low solar illumination. Their findings indicated that some individual measurements exhibited more significant overshoots than those found in earlier studies, surpassing theoretical predictions. A potential reason for this discrepancy might be the different dust-charging conditions, which could stem from reduced solar illumination around midnight or from long-term variations in ice particles present in the mesosphere. Recently, Mahmoudian et al. (2020) introduced an innovative approach to study dust charging in the region responsible for PMSE. This technique involved high-frequency modulation of the PMSE, utilizing various levels of pump power, and was carried out during a recent experimental campaign at EISCAT.

This paper presents, for the first time, the response of the coherent VHF PMSE spectrum to HF radio wave modulation under two distinct experimental configurations. Data from power-stepping modulation (24 July 2019) and power-sweeping modulation (26 July 2019) experiments are analyzed to investigate the spectral contraction of radar echoes during heating. These contractions are attributed to the dominance of electron diffusion in suppressing electron density irregularities. The simultaneous behavior of PMSE at two altitude layers and their respective responses to HF pump modulation are also examined. Additionally, a numerical simulation framework is employed to explore radar echo characteristics as a function of dusty plasma parameters. Dust cloud properties specific to each heating cycle are inferred through comparison between observational data and simulation results. Information on electron temperature elevation, derived from coherent spectral analysis, is incorporated to constrain model parameters. The agreement between the numerical results and the proposed hypothesis regarding the coherent spectrum's sensitivity to HF pump modulation is evaluated. A summary of the key findings and concluding remarks are provided at the end.

2 Numerical Model

73

75

76

78

79

80

82

83

84

86

87

90

91

92

93

95

96

98

101

102

103

104

105

106

107

109

110

111

A hybrid computational model is employed to examine the temporal dynamics of irregularities during the active modification of PMSE (Scales and Chen, 2008; Chen and Scales,

2005). This model characterizes electrons and ions using fluid equations, while dust is represented through simulation particles via the Particle-In-Cell (PIC) approach. The changes in ion density are articulated through the continuity equation. The mesopause temperature for both ions and electrons is set at $T_e = T_i = 150 \text{ K}$. At the PMSE height range, proton hydrates with masses ranging from 59 to 109 proton masses are the predominant ion compositions. O_2^+ ions outnumber NO^+ ions, and in combination, NO^+ and O_2^+ can be slightly denser than proton hydrates at altitudes of 88 km and above (Kopp et al., 1985). It's important to point out that fluctuations in ion mass from 50 to 100 proton masses do not significantly affect the evolution of irregularity amplitude during heating. The ion-neutral collision frequency is estimated to be around 10⁵ s⁻¹ (Lie-Svenson et al., 2003). Predictions suggest that this frequency varies between 3×10^4 s¹ and 3×10^5 s¹ within the altitude range of 80–90 km (Turunen et al., 1988), and this paper examines its impact on irregularity amplitude during active modification. We focus on the temporal behavior of charged dust related to electron irregularities that occur during electron temperature increases resulting from radio wave heating. The model incorporates the effects of temperature on the electron-neutral collision frequency and the recombination rate coefficient. It is assumed that the collision frequency varies with temperature as $\nu_{en} \sim T_e$, while the dependence of the recombination rate is modeled as $\alpha \sim$ $T_e^{1/2}$. The charging of dust particles is described using a standard continuous charging model. Research by Chen and Scales (2007) indicates that a discrete charging model behaves similarly to a continuous one for dust grains of relatively small size at PMSE altitudes. Additionally, the charge on each dust particle changes over time according to the Orbital-Motion-Limited (OML) approach as outlined by Shukla and Mamun (2002).

3 Experiment setup

The HF pump modulation campaign took place from July 22 to July 26, 2019, at the EISCAT facility close to Tromsø, in northern Norway. Each day, the experiments were initiated around 7:00 UT and continued until approximately 13:00 UT, depending on the mesospheric conditions and the presence of a PMSE layer. The VHF data discussed here boasts a vertical resolution of 300 meters and a time resolution of 4.8 sec, which reflects the integration time of the radar echo's autocorrelation functions. A pulse-to-pulse correlation modulation scheme was implemented, using the HF facility to heat electrons in the mesosphere while conducting VHF radar observations (Rietveld et al., 2016). Over the three days highlighted, ten transmitters operated with Antenna Array 1 at a frequency of 6.2 MHz, employing a vertical beam and X-mode.

July 24, 2019: On July 24, the HF experiment utilized X-mode heating, leading to impressive PMSE modulation, which will be elaborated on shortly. During the first part of the day, power output was adjusted to levels of 40, 60, and 80 kW, and in the final hour, it shifted to 10, 20, 40, 60, and 80 kW for each new heating cycle. The nominal power levels of 20, 40, 60, and 80 kW for these cycles yield effective radiated powers (total transmitter power multiplied by antenna array gain, ERP) of roughly 52, 114, 240, 380, and 485 MW, respectively, assuming a perfectly conducting ground. The heater was activated for 48 sec, followed by a 120-sec off period.

July 26, 2019: On the final day of our experiment, we observed a continuous increase in heating power throughout the cycle. The VHF radar began operating at 07:00 UT and continued until the scheduled conclusion at 11:00 UT. During this period, we detected PMSE echoes, which remained stable for the initial two hours, though their strength was moderate. The 62.4-sec heater cycle with linear power sweeping commenced at 07:19 UT, while the HF experiment utilized X-mode heating once more. In the first two hours, the HF heater executed a linear power sweep, gradually ramping up from zero to full power over the 62.4 sec. This was followed by a 144-sec off period, resulting in a complete cycle of 206.4 sec. To ensure a scientifically robust design for investigating the dust charging process in the Earth's middle atmosphere, we employed a quasi-continuous power

stepping method, which involved numerous small adjustments every 0.515 sec, rather than relying on basic on/off cycles. Specifically, the power across the ten heating transmitters was elevated in 120 increments (corresponding to the 62.4-sec on period), reaching a nominal 80 kW per transmitter, followed by a 144-sec off phase. At approximately 09:02 UT, the experimental protocol was modified to match the power stepping program used on July 25. During the latter half of the run, we noted that the VHF PMSE echoes became weaker and more variable, with some instances of complete absence.

4 Results

One way of understanding the response of the electron density fluctuation amplitude to the background dust plasma parameters is to use the analytical expression for the timescale of physical processes that actually affect the density fluctuations. In general two processes of charging (electron/ion attachment to the dust particles) and plasma density diffusion determine the steady state amplitude of fluctuations in the plasma density. The diffusion process tends to smooth out irregularities and can be approximated for the natural PMSE layer ($T_e/T_i=1$) by (Chen and Scales, 2005; Mahmoudian et al., 2011, 2017, 2018, 2020):

$$\tau_{diff} \approx \left(\frac{\lambda_{irreg}}{2\pi}\right) \frac{1}{\frac{KT_i}{m_i \nu_{in}} (1 + r_h) \left(1 + \frac{z_{d0} n_{d0}}{n_{e0}}\right)} \tag{1}$$

where ν_{in} , z_{d0} , λ_{irreg} and v_{thi} are the ion-neutral collision frequency, charge density on the dust particles, electron density irregularity wavelength and ion thermal velocity, respectively. According to the theoretical expression of diffusion time scale this is mainly due to the dependency of diffusion time scales on λ_{irreg} .

The timescale for electron attachment onto the dust is approximated by

$$\tau_{chg} = \frac{1}{|\langle I_e + I_i \rangle|} \approx \frac{1}{\sqrt{8\pi} r_d^2 v_{te0} e^{\frac{\phi}{r_h}} \sqrt{r_h}}$$
 (2)

While such simple theoretical expressions predict the dependency of radar echoes on the background dusty plasma parameters, they are unable to predict the time evolution nor steady state amplitude of irregularities (δn_e^2) responsible for radar echoes. Therefore, a complicated computational model is incorporated in this paper to study the characteristics of radar echoes with respect to the dusty plasma parameters. As can be seen in Eq. (1), the diffusion timescale depends on the λ_{irreg} . The numerical simulations presented in this paper are associated with radar frequencies slightly different from the observations due to a limitation of the model having a discrete spatial grid. The difference is of the order of a few centimeters in fluctuation wavelength, and are not expected to change the physical processes and the results.

In this section, results of the power-stepping on July 24, and the power-sweeping modulation on July 26, will be presented.

4.1 Experiment 1: July 24, 2019

On this day, the HF pump power was varied between 40kW, 60kW, and 80kW. Each power level was applied for 48 sec, followed by a heater-off period lasting 120 sec. Figure 1 presents the backscattered VHF signal recorded during five heating cycles between 09:15 and 10:00AM. Two distinct PMSE layers are clearly visible throughout these cycles. Changes in the separation distance between the upper and lower layers are also evident; for example, cycles 1 and 2 exhibit the greatest separation, while the layers appear closer together in

cycles 4 and 5. The modulation effects on these two layers are examined in detail for cycles 1, 3, and 5 in the following sections.

cycle 1: cycle 1 began at 09:18:44 UT with HF pump modulation at 40kW. The upper layer expanded from 83.07km to 84.15km, while the lower layer ranged between 87.7km and 88.4km. As shown in Figure 1, weak modulation of the VHF PMSE is observed for both layers at this power level. Modulation at 60kW started at 09:21:32 UT. Compared to the 40kW cycle, both layers appear thinner, but the reduction in VHF PMSE strength is significantly greater. Finally, the 80kW modulation began at 09:24:20 UT. During this period, the lower layer exhibits a noticeable downward shift, with its center around 83km, while the upper layer remains approximately at the same altitude as in previous heating periods. However, the natural PMSE intensity in the upper layer weakens substantially. Both layers display a pronounced weakening of the echo during the modulation.

cycle 3: Among the five cycles shown in Figure 1, cycle 3 exhibits the weakest natural PMSE in both the upper and lower layers. Additionally, the two layers are noticeably closer to each other compared to cycle 1, especially during the 40kW modulation. This cycle begins with the 40kW modulation at 09:35:32 UT. The center of the lower layer is at 84.5km, while the upper layer is centered at 87.03km. Similar to cycle 1, only weak modulation is observed at this power level. The 60kW modulation started at 09:38:20 UT. Here, the layers are more separated than during the 40kW modulation, but still closer than in cycle 1, with the lower layer center at 84.15km and the upper layer at 87.7km. The upper layer also exhibits a notably small thickness during this period. The final modulation for this cycle, at 80kW, began at 09:41:08 UT. As in cycle 1, the strongest echo weakening occurred at this power. The centers of the lower and upper layers remain at approximately 84.15km and 87.7km, respectively.

cycle 5: Finally, the last cycle studied here is cycle 5. This cycle exhibits the strongest natural PMSE, with the layer thickness greater than in the other cycles. Notably, the lower layer experiences more pronounced modulation than the upper layer. The cycle began with 40kW modulation at 09:52:20 UT, with the lower layer centered at 83.7km and the upper layer at 87.03km. The 60kW modulation started at 09:55:08 UT, during which the lower layer center shifted slightly down to 83.4km, while the upper layer remained at 87.03km. The final modulation at 80kW commenced at 09:57:56 UT. As with the other cycles, the 80kW power produced the strongest modulation in both layers. A detailed comparison of the modulation amplitudes for different power levels, as well as between the upper and lower layers, is presented in the normalized echo power analysis that follows.

To analyze the modulation effects of different HF pump powers on echo strength and to compare the responses of the upper and lower PMSE layers for cycles 1, 3, and 5, the VHF radar echoes were normalized to the echo levels recorded just before the HF heater was activated. Figures 2 and 3 present the normalized PMSE echoes for the three stepped power levels (40, 60, and 80kW). In these figures, the red lines correspond to the upper layer, while the lower lines represent the bottom layer. In Figure 2, the left column corresponds to cycle 1 and the right column to cycle 3.

The normalized echoes in Figures 2 and 3 show consistent behavior across the three cycles displayed in Figure 1, exhibiting similar suppression amplitudes, turn-off overshoot, and relaxation times at the different HF power levels. Across all three cycles, the 80kW power produces the strongest modulation in both layers, consistent with the observations in Figure 1.

Some differences in modulation patterns between the two layers within the same heating power are noteworthy. For example, Figure 2a shows nearly identical modulation patterns for 40kW, but the lower layer exhibits a larger turn-off overshoot. In Figure 2b, the lower layer experiences stronger modulation than the upper layer, although both lay-

ers show similar turn-off overshoot. Figure 2c presents an interesting case at 80kW: the lower layer initially shows a steeper modulation slope than the upper layer, but after some time, the upper layer exhibits stronger modulation. The lower layer also has a significantly larger turn-off overshoot. Figures 2d–2f display normalized echoes for cycle 3, where all power levels show greater modulation in the lower layer compared to the upper layer. Surprisingly, the difference between the layers' modulation is most pronounced at 40kW. Finally, Figures 3a–3c, illustrating normalized echoes for cycle 5, reveal that at 40kW and 80kW, the lower layer modulation exceeds that of the upper layer, while at 60kW, both layers exhibit nearly identical modulation levels.

Another interesting aspect to investigate is the effect of HF modulation on the VHF PMSE spectrum. Figure 4 displays the VHF PMSE spectra at two time points—before modulation and immediately after heating is turned on—for both the upper and lower layers (left and right columns, respectively) at three power levels (40, 60, and 80kW) during cycle 1. In all cases, the spectral width and amplitude are greater before modulation than after heating begins. This observation aligns with the explanation that, following heater activation, enhanced diffusion reduces electron density irregularities, leading to fewer scatterers and consequently narrower spectral widths.

To better visualize the modulation effects on the spectrum, Figure 5a–5c show the normalized area under the spectral curve over 48 sec for cycles 1 and 5. Dashed lines represent cycle 5, solid lines represent cycle 1, and red and blue colors correspond to the upper and lower layers, respectively. A notable feature across all power levels is a sharp contraction of the spectrum immediately after heater activation, followed by a relatively stable area with small fluctuations throughout the remainder of the modulation period. Another key point is that the degree of spectral contraction increases with pump power, with the greatest contraction observed at 80kW.

4.2 Experiment 2: July 26, 2019

On this day, as previously mentioned, the HF power was swept linearly over 62.4 sec, followed by a 44-sec off period, resulting in a complete cycle duration of 206.4 sec. Figure 6 shows the backscattered VHF signal recorded between 08:10:43 UT and 08:41:41 UT. Initially, the PMSE layer is centered around 82.7km with a thickness of approximately 3km. Between 08:21:02 UT and 08:24:29 UT, an upward motion of the layer is observed. Afterward, the center stabilizes near 84.15km with a significantly reduced thickness of about 1km and remains constant until 08:41:41 UT. Solid white lines in the figure indicate heater-on periods. Nine heating cycles are evident during this time span. Among these, cycles 2, 3, 4, and 9 were selected to analyze the modulation effects on both the echoes and the spectra.

Modulations due to HF heating are observable in all these cycles. Notably, a gradual weakening of the backscattered signal occurs throughout nearly all cycles, consistent with expectations from power sweeping. This contrasts with the power stepping experiments, where a sharp decrease in echo power was seen immediately after heater activation, followed by a relatively stable period. To better illustrate this gradual weakening, Figure 7 presents the normalized echo amplitudes for these four cycles. Despite some fluctuations during the power sweep, all four cycles show a general decreasing trend in echo power, with cycle 4 exhibiting the smoothest decline. cycle 3, however, demonstrates the strongest modulation.

Now, we focus on the response of the PMSE spectrum to this experimental setup. We expect to observe a gradual contraction of the spectrum over time. To investigate this, the spectra for the four selected cycles are shown at three time points: 0 sec (before heating), 28.8 sec, and 57.6 sec, represented by red, blue, and black lines, respectively, in Figure 8. For all cycles, a progressive decrease in both the spectral width and amplitude is evident as time advances. Furthermore, to better illustrate this gradual effect, the area

under the spectrum over the 62.4-sec heating period is plotted in Figure 9. This clearly demonstrates a gradual decrease in the spectral area, with some fluctuations, consistent with our expectations. Similar to the normalized echo power shown in Figure 7, cycle 4 exhibits the smoothest decline in spectral area, while cycle 3 shows the most pronounced reduction as time progresses.

5 Discussion

As discussed previously, under conditions of constant HF pump power during the heating "on" period, the area under the spectral curve decreases and then stabilizes. Figure 4 presents VHF PMSE spectra at two time points—immediately before modulation and just after heater activation—for both the upper (left panel) and lower (right panel) layers observed on July 24, 2019. The top, middle, and bottom panels correspond to HF pump powers of 40 kW, 60 kW, and 80 kW, respectively. A clear narrowing of the VHF spectrum is observed following heater turn-on. Figure 5 shows this behavior for both the up and down layers during heating cycles 3 and 5, where the spectral area remains relatively stable with minor fluctuations throughout the remainder of the modulation period. The amplitude of electron density fluctuations—responsible for the coherent VHF echoes—is governed by two primary physical processes: diffusion and dust charging. Diffusion tends to suppress the fluctuation amplitude, while enhanced dust charging, due to increased electron temperatures, can amplify it. Additionally, dust density fluctuations driven by neutral air turbulence can further enhance electron density fluctuations through the charging process.

Equations (1) and (2) describe the characteristic timescales of the diffusion and charging processes. These timescales—and their ratio $\tau_{\rm diff}/\tau_{\rm chg}$ —depend on background dust and plasma parameters, as well as the heating ratio (T_e/T_i) . Given the short duration of each heating cycle, background conditions can be considered constant, with HF pump power being the primary variable. In the July 24 experiments, the pump power remained constant during each individual cycle. The observed reduction and stabilization of the spectral area reflect this influence. Minor recoveries observed during some heating periods may be attributed to modifications in the recombination rate, which will be discussed alongside numerical results. The observed correlation between decreasing spectral area and increasing pump power further supports the interpretation that diffusion-induced suppression of electron density fluctuations is reflected in the spectral response.

To evaluate the proposed relationship between the area under the coherent spectrum and HF pump power, this method was applied to the experimental data from July 26, 2019. Figure 8 presents the spectral profiles for four selected heating cycles at three distinct time points: 0 sec (pre-heating), 28.8 sec, and 57.6 sec, indicated by red, blue, and black lines, respectively. A clear suppression of the spectral area is observed as the heating cycle progresses, corresponding to increased HF pump power. This validates the relationship between heating ratio and reduced fluctuation near VHF wavelength that can be justified with ratio $\tau_{\rm diff}/\tau_{\rm chg}$. Figure 9 shows normalized area under the spectral curve over a 62.4-sec interval for 4 selected heating cycles on July 26, 2019. The dashed line represents the ratio $\tau_{\rm diff}/\tau_{\rm chg}$, calculated from Equations (1) and (2) using a stepwise increase in the heating ratio (T_e/T_i) every 4.8 sec during the heating cycle. A continuous decrease in the normalized spectral area is observed as the HF pump power increases, aligning with the evolution of $\tau_{\rm diff}/\tau_{\rm chg}$. These results support the hypothesis that the area under the coherent spectrum serves as an indirect indicator of the heating ratio T_e/T_i during HF heating.

The primary trend observed in the normalized radar echo amplitude aligns with the gradual decay in the area under the coherent spectrum curve. This behavior is consistent with a slow increase in electron temperature relative to the background ion temperature (r_h) , and in agreement with the theoretical expectations from expressions (1) and (2), corresponding to diffusion and charging timescales, respectively. Specifically, a gradual decline in the ratio $\tau_{\rm diff}/\tau_{\rm chg}$ is expected, indicating that the relative timescales of diffusion and charging govern the amplitude of density fluctuations.

Table 1 summarizes the area under the coherent spectrum curve for heating cycles 1, 3, and 5, both immediately before and 4.8 sec after the HF-heater is activated. These results encompass both the up and down layers, with values grouped according to heating cycle and HF pump power. Table 2 presents the corresponding ratios of spectral area decrease following heater activation. A clear decreasing trend in the ratio of spectral area reduction is observed with increasing pump power, consistent with the influence of diffusion and charging dynamics governed by the heating ratio (T_e/T_i) . Interestingly, the reduction in spectral area relative to the natural (unheated) layer is less pronounced in the down layer, suggesting that the heating effect is stronger at lower altitudes compared to higher-altitude layers. Furthermore, the spectral contrast becomes more prominent as the pump power increases from 40 kW to 80 kW. These observations impose constraints on the T_e/T_i ratio that must be incorporated into numerical simulations to achieve consistency with experimental data. Adopting this approach will enhance the accuracy of dust cloud parameter estimation while narrowing the range of input parameters required in the computational model.

To investigate the parameters and temporal evolution of dust/ice cloud formation, observational data are compared with numerical simulations. The model explores a wide range of scenarios, varying dust radius, density, and the heating ratio (r_h) . The primary objective is to constrain the heating ratio by analyzing the area under the spectral curve, which correlates with the applied heating power. A consistent increase in the electronto-ion temperature ratio (T_e/T_i) is observed across heating cycles of 40, 60, and 80 kW. The optimal dust parameters are determined by identifying the simulation that best matches the observational data.

Figure 10 represents the simulation results associated with dust radius (r_d) of 3 nm. Panels (a) through (c) correspond to background dust density variation with respect to electron density (n_d/n_{e0}) of 90%, 110%, and 150%. The recombination rate is 0.1. The heating ratio (T_e/T_i) is varies from 1.25 to 3. The radar frequency is 224 MHz. The dust density fluctuation amplitude $\delta n_d/\delta n_{d0}$ is 0.5. The color and line style corresponding to each T_e/T_i values is assumed to be the same in all panels. At lower dust density of $n_d/n_{e0}=90\%$, the normalized radar echo amplitude reduces to 0.6 and the turn-off overshoot varies between 1.2 to 2.4 as the T_e/T_i ratio increases from 1.25 to 3 during HF-pump heating. As the dust density n_d/n_{e0} increases to 110% and 150%, the normalized radar echo shows a deeper reduction during heating with a suppressed turn-off overshoot. The maximum turn-off overshoot reduced to 1.8 and \sim 1.3 in the case of $n_d/n_{e0}=110\%$ and 150%, respectively. The results are summarized in Table 3.

Figure 11 presents simulation results for larger dust grain radii of 5 nm and 10 nm. Dust number densities are varied at 20%, 40%, 60%, and 80% relative to the initial electron density (n_d/n_{e0}) , with a fixed heating ratio (T_e/T_i) of 2 in all cases. The right-hand panel of the figure shows results incorporating an enhanced recombination rate, increased by a factor of four. The recombination process is modeled using the expression $L_i = \alpha n_e n_i$, where $\alpha = 10^{-12} \, \mathrm{m}^3 \mathrm{s}^{-1}$ represents the recombination rate coefficient characteristic of mesospheric altitudes. The simulations indicate that recombination primarily influences the recovery of the suppressed radar echo during HF-pump heating. An increase in α by a factor of four results in a significant enhancement in the recovery of fluctuation amplitude, suggesting that recombination plays a critical role in post-heating echo dynamics. These recombination effects will be incorporated into further modeling efforts to achieve optimal agreement with observational data, particularly for the up layer during heating cycle 3. As can be seen, at higher dust densities and larger dust radius the normalized radar echo amplitude reaches zero and turn-off overshoot barely passes its initial amplitude before heater turn-on. For the sinusoidal perturbations used in this work to model

the irregularities, the radar reflectivity (η_k) is proportional to $(\delta n_e)^2$ where δn_e is the electron irregularity amplitude.

410

411

412

413

414

415

416

417

419

420

421

423

427

428

431

432

433

435

436

439

440

443

444

445

446

448

449

450

451

452

453

455

456

457

459

460

During heating cycle 1, under low HF pump power (40 kW), the normalized radar echo amplitudes reach 0.5 and 0.4 for the upper and lower layers, respectively. In this case, the lower layer exhibits a turn-off overshoot of approximately 1.3. The VHF echo associated with the upper layer shows significant weakening during the turn-off period, making it difficult to quantify a clear overshoot. At an intermediate pump power of 60 kW, the upper and lower layers show minimum turn-on amplitudes of 0.4 and 0.2, with corresponding turn-off overshoot amplitudes of 1.4 and 1.6, respectively. At the highest pump power (80 kW), the lower layer exhibits a turn-on minimum of 0.2 and a turn-off overshoot of 1.9. Due to reduced modulation effects and nonlinear echo behavior, no reliable minimum or overshoot values could be determined for the upper layer at this power level. Numerical simulations closely matching these observations suggest a dust radius of 5 nm for both the upper and lower layers. The best-fit dust densities are 70% and 80% of the background electron density for the upper and lower layers, respectively. The corresponding heating ratios (T_e/T_i) obtained from the simulations are 1.8, 2.0, and 2.2, consistent with the observed trend of enhanced temperature effects influencing the VHF spectral response.

During heating cycle 3, the VHF echo exhibits distinct signatures at both the upper and lower layers. In the upper layer, a gradual recovery is observed following the initial amplitude reduction immediately after HF pump activation. The minimum normalized echo amplitudes reach 0.5, 0.4, and 0.3 for HF pump powers of 40 kW, 60 kW, and 80 kW, respectively. Corresponding turn-off overshoot amplitudes reach 2.0, 2.4, and 1.6. Partial recovery to amplitudes of 0.8 and 0.55 is observed at 40 kW and 60 kW, respectively. Numerical simulations that best match these observations indicate dust parameters of radius $r_d = 5$ nm and relative density $n_d/n_{e0} = 60\%$ for the upper layer. The corresponding heating ratios (T_e/T_i) derived from the simulations are 1.8, 2.0, and 2.2, consistent with the trend of increased electron temperature effects observed in the VHF spectral profiles. An enhanced recombination rate of 0.2 and 0.15 was required to match the observations at 40 kW and 60 kW, respectively.

In the lower layer, the normalized echo amplitudes decrease to 0.4, 0.3, and 0.2 for increasing HF pump powers of 40 kW, 60 kW, and 80 kW, respectively, with corresponding turn-off overshoot amplitudes of 1.4, 1.4, and approximately 1.0. Numerical modeling that reproduces this behavior suggests dust parameters of $r_d = 3$ nm and $n_d/n_{e0} = 150\%$ for the lower layer. The best-fit heating ratios (T_e/T_i) in this case are 2.25, 2.5, and 3, further supporting the observed trend of temperature-enhanced diffusion effects in the VHF spectral response.

During heating cycle 5, the down layer exhibits a minimum normalized amplitude of 0.4, 0.3, and 0.18 following heater activation, corresponding to pump powers of 40, 60, and 80 kW, respectively. The reduced echo remains at a nearly constant amplitude throughout the heating cycle. Upon heater turn-off, an overshoot in the down layer is observed, with peak amplitudes of 1.2, 1.5, and approximately 1.15 for increasing pump powers. In comparison, the upper layer demonstrates a more moderate response during heater turn-on, with amplitude suppressions of 0.5, 0.3, and 0.2 at pump powers of 40, 60, and 80 kW, respectively. A turn-off overshoot of 2, ~1.5, 1.1-1.2 is observed. The comparison with numerical simulations reveal that the parameters associated with the down layer are $n_d/n_{e0} = 150\%$, $r_d = 3$ nm, and recombination rate = 0.1. The heating ratios (T_e/T_i) shows an increasing trend of 2.25, 2.5 and 3 associated with increasing pump power of 40 kW, 60 kW, and 80 kW. This is also consistent with the general behavior observed in the VHF spectral response to increasing HF-pump power. The closest numerical results to match the observations at the up layer reveal dust parameters of $n_d/n_{e0} = 110\%$, $r_d = 3$ nm, and recombination rate = 0.1. Overall, the general trend obtained through comparison of numerical simulations and observations show that both layers start with

lower dust density $\sim 70-80\%$ and larger dust particles 5 nm in heating cycle 1. Later on, in heating cycle 3 the radar echoes are consistent with numerical results of smaller dust size of 3 nm and larger dust density 150%. The upper layer remains populated with larger dust of 5 nm and slightly lower density in heating cycle 3. During heating cycle 5, both layer show to be populated with small dust size of 3 nm and high densities of 110% and 150% at up and down layers, respectively. This observation is consistent with the prevailing hypothesis that dust and ice particles responsible for PMSE formation originate at higher altitudes near the upper boundary of the PMSE source region. Initially forming as nanometer-sized charged clusters, these particles grow through processes such as condensation and coagulation, subsequently increasing in mass and descending to lower altitudes within the mesosphere (Rapp and Lübken, 2000; Havnes et al., 1996). The vertical transport is influenced by gravitational settling, ion drag, and background turbulence, which together shape the vertical distribution and layering of the dust population. As these particles grow in size, their interaction with the ambient plasma becomes more effective, enhancing the conditions necessary for radar backscatter and influencing the altitude-dependent structure of PMSE layers (Lie-Svendsen et al., 2003; Rapp et al., 2004). These processes play a critical role in the temporal and spatial evolution of PMSE and are essential for interpreting observations of layer descent and spectral modifications during heating experiments.

6 Summary and Conclusion

463

464

465

468

469

470

471

472

475

476

477

478

479

480

481

483

484

488

489

490

492

493

494

495

496

497

500

501

504

505

506

507

508

510

512

513

514

This study presents detailed observations and numerical modeling of the coherent VHF radar spectral response to high-frequency (HF) pump power modulation in the presence of polar mesospheric summer echoes (PMSE). Two experimental configurations were analyzed: a power-stepping modulation on 24 July 2019 and a power-sweeping modulation on 26 July 2019. The results demonstrate a clear correlation between increasing HF-pump power and suppression of the VHF spectral area, consistent with enhanced electron temperature and dominant diffusion processes affecting electron density irregularities.

Specifically, this study investigates the response of VHF coherent radar echoes from PMSE to HF pump heating using both experimental observations and numerical simulations. Systematic analysis reveals that the area under the VHF spectral curve consistently decreases during HF heating, with the degree of suppression correlating with increased HF pump power (40–80 kW). This spectral narrowing is attributed to enhanced diffusion processes and dust charging effects caused by elevated electron temperatures. The ratio of characteristic diffusion and charging timescales ($\tau_{\rm diff}/\tau_{\rm chg}$) derived from theoretical expressions is used to interpret the observed echo suppression and its evolution during modulation.

Distinct responses were observed in both upper and lower PMSE layers, with measurable differences in minimum echo amplitudes and turn-off overshoots. These variations were successfully interpreted using numerical simulations that incorporated dust cloud parameters such as particle radius and relative dust density. Best-fit simulations yielded T_e/T_i ratios ranging from 1.8 to 3.4, which aligned well with observed spectral trends. Additionally, enhanced recombination rates were introduced to match specific cases, further improving model consistency with measurements. Experimental results from multiple heating cycles demonstrate layer-specific responses, with the lower layer showing greater overshoot amplitudes and more stable post-heating echoes. Through close comparison with simulations, optimal dust cloud parameters—radius, density, and recombination rate—are determined for each case. The best-fit models indicate increasing heating ratios (T_e/T_i) with pump power, supporting the interpretation of temperature-driven modulation in echo strength. Specifically, lower layers are associated with higher dust densities and smaller grain sizes, while upper layers show a trend of larger particles and initially lower dust densities. The observed evolution of dust parameters across heating cycles is consistent with the hypothesis that PMSE-related ice particles originate at higher

- altitudes and descend over time as they grow in size. These findings reinforce the role
- of dusty plasma dynamics in shaping the spectral and spatial structure of PMSE dur-
- ing active HF modulation, providing new constraints for modeling mesospheric turbu-
- lence and dust cloud evolution.
- The agreement between experimental data and numerical results supports the hypoth-
- esis that the area under the coherent spectrum serves as an indirect proxy for estimat-
- ing electron temperature enhancements during HF heating. This work reinforces the util-
- 522 ity of spectral diagnostics in PMSE studies and provides a framework for future inves-
- tigation into dusty plasma dynamics in the polar mesosphere.

Acknowledgments

524

527

- 525 The authors would like to thank EISCAT Scientific Association and staff for their help
- to run this experiment.

Open Research

- The original numerical model used in this research is developed at Virginia Tech. The
- numerical results are available upon request.

References

- Belova, E., P.B. Chilson, S. Kirkwood, and M.T. Rietveld, "The response time of PMSE
- to ionospheric heating," Journal of Geophysical Research (Atmospheres), vol. 108, no.
- D8, pp. PMR 13-1-PMR 13-6, 2003, doi:10.1029/2002JD002385.
- Biebricher, A., Havnes, O., Hartquist, T., and LaHoz, C.: On the influence of plasma
- absorption by dust on the PMSE overshoot effect, Adv. Space Res., 38, 2541–2550, 2006.
- Bremer, J., P. Hoffmann, A. H. Manson, C. E. Meek, R. Rüster, and W. Singer (1996),
- PMSE observations at three different frequencies in northern Europe during summer 1994,
- Ann. Geophys., 14, 1317–1327.
- Chau, J. L., McKay, D., Vierinen, J. P., La Hoz, C., Ulich, T., Lehtinen, M., and Lat-
- teck, R.: Multi-static spatial and angular studies of polar mesospheric summer echoes
- combining MAARSY and KAIRA, Atmos. Chem. Phys., 18, 9547–9560, https://doi.org/10.5194/acp-
- 18-9547-2018, 2018.
- Chen, C., & Scales, W. A. (2005). Electron temperature enhancement effects on plasma
- irregularities associated with charged dust in the Earth's mesosphere. Journal of Geo-
- physical Research, 110, A12313. https://doi.org/10.1029/2005JA011341
- Chilson, P. B., Belova, E., Rietveld, M. T., Kirkwood, S., & Hoppe, U. (2000). First ar-
- tificially induced modulation of PMSE using the EISCAT heating facility. Geophysical
- 548 Research Letters, 27, 3801–3804.
- ⁵⁴⁹ Cho, J. Y. N., & Rottger, J. (1997). An updated review of polar mesosphere summer
- echoes: Observation, theory, and their relationship to noctilucent clouds and subvisible
- aerosols. Journal of Geophysical Research, 102, 2001–2020.
- Ecklund, W. L., & Balsley, B. B. (1981). Long-term observations of the Arctic mesosphere
- with the MST radar at Poker Flat, Alaska. Journal of Geophysical Research, 86, 7775–7780.
- Havnes, O., Trøim, J., Blix, T., Mortensen, W., Næsheim, L.I., Thrane, E., Tønnesen,
- T. (1996). First detection of charged dust particles in the Earth's mesosphere. Journal
- of Geophysical Research, 101, 10839–10847. https://doi.org/10.1029/96JA00003

- Havnes, O., La Hoz, C., Nsheim, L. I., & Rietveld, M. T. (2003). First observations of
- the PMSE overshoot effect and its use for investigating the conditions in the summer meso-
- sphere. Geophysical Research Letters, 30(23), 2229. https://doi.org/10.1029/2003JA010159
- Havnes, O., Pinedo, H., La Hoz, C., Senior, A., Hartquist, T. W., Rietveld, M. T., & Kosch,
- M. J. (2015). A comparison of overshoot modeling with observations of polar mesospheric
- summer echoes at radar frequencies of 56 and 224 MHz. Annales de Geophysique, 33,
- 563 737–747. https://doi.org/10.5194/angeo-33-737-2015
- Gunnarsdottir, T. L., Poggenpohl, A., Mann, I., Mahmoudian, A., Dalin, P., Haeggstroem,
- I., and Rietveld, M.: Modulation of polar mesospheric summer echoes (PMSEs) with high-
- frequency heating during low solar illumination, Ann. Geophys., 41, 93–114, https://doi.org/10.5194/angeo-
- 41-93-2023, 2023.
- La Hoz, C., and O. Havnes (2008), Artificial modification of polar mesospheric winter
- echoes with an RF heater: Do charged dust particles play an active role?, J. Geophys.
- 8570 Res., 113, D19205, doi:10.1029/2008JD010460.
- Mahmoudian, A., Scales, W. A., Kosch, M. J., Senior, A., and Rietveld, M.: Dusty space
- plasma diagnosis using temporal behavior of polar mesospheric summer echoes during
- active modification, Ann. Geophys., 29, 2169–2179, https://doi.org/10.5194/angeo-29-
- 2169-2011, 2011.
- Mahmoudian, A., and W.A. Scales, On the signature of positively charged dust parti-
- cles on plasma irregularities in the mesosphere, Journal of Atmospheric and Solar-Terrestrial
- Physics, 104, 2013, 260-269, https://doi.org/10.1016/j.jastp.2012.12.002.
- Mahmoudian, A., Mohebalhojeh, A. R., Farahani, M. M., Scales, W. A., & Kosch, M.
- 579 (2017). Remote sensing of mesospheric dust layers using active modulation of PMWE
- by high-power radio waves. Journal of Geophysical Research: Space Physics, 122, 843–856.
- https://doi.org/10.1002/2016JA023388
- Mahmoudian, A., Senior, A., Scales, W. A., Kosch, M. J., & Rietveld, M. T. (2018). Dusty
- space plasma diagnosis using the behavior of polar mesospheric summer echoes during
- electron precipitation events. Journal of Geophysical Research: Space Physics, 123, 7697–7709.
- https://doi.org/10.1029/2018JA025395
- Mahmoudian, A., Kosch, M. J., Vierinen, J., & Rietveld, M. T. (2020). A new technique
- for investigating dust charging in the PMSE source region. Geophysical Research Let-
- ters, 47, e2020GL089639. https://doi.org/10.1029/2020GL089639
- Mahmoudian, A., Kosch, M. J., Scales, W. A., Rietveld, M. T., & Pinedo, H. (2022). Neu-
- tral air turbulence in the mesosphere and associated polar mesospheric summer echoes
- ⁵⁹¹ (PMSEs). Radio Science, 57, e2021RS007371. https://doi.org/10.1029/2021RS007371
- Pinedo, H., C. La Hoz, O. Havnes, and M. Rietveld (2014), Electron-ion temperature
- ratio estimations in the summer polar mesosphere when subject to HF radio wave heat-
- ing, J. Atmos. Sol. Terr. Phys., 118, 106–112, doi:10.1016/j.jastp.2013.12.016.
- Rapp, M., and F.-J. Lübken (2000), Electron temperature control of PMSE, Geophys.
- Res. Lett., 27, 3285–3288.
- Rapp, M., & Lubken, F. J. (2004). Polar mesosphere summer echoes (PMSE): Review
- of observations and current understanding. Atmospheric Chemistry and Physics, 4, 2601–2633.
- Rishbeth, H., and A. P. van Eyken (1993), EISCAT—Early history and the first ten years
- of operation, J. Atmos. Terr. Phys., 55(4–5), 525–542.
- Rietveld, M., Kohl, H., Kopka, H., and Stubbe, P.: Introduction to ionospheric heating
- at Tromsø—I. Experimental overview, J. Atmos. Sol.-Terr. Phy., 55, 577–599, 1993.

- Scales, W. (2004). Electron temperature effects on small-scale plasma irregularities as-
- sociated with charged dust in the Earths mesosphere. IEEE Transactions on Plasma Sci-
- ence, 32, 724.
- Scales, W. A., & Mahmoudian, A. (2016). Charged dust phenomena in the near Earth
- space environment. Reports on Progress in Physics, 79(10), 106802. https://doi.org/10.1088/0034-
- 4885/79/10/106802
- Senior, A., Mahmoudian, A., Pinedo, H., La Hoz, C., Rietveld, M. T., Scales, W. A., &
- Kosch, M. J. (2014). First modulation of high-frequency polar mesospheric summer echoes
- by radio heating of the ionosphere. Geophysical Research Letters, 41, 5347–5353. https://doi.org/10.1002/2014GI
- 512 Sommer, S. and Chau, J. L.: Patches of polar mesospheric summer echoes characterized
- from radar imaging observations with MAARSY, Ann. Geophys., 34, 1231–1241, https://doi.org/10.5194/angeo-
- 34-1231-2016, 2016.

Area under the curve						
		Heating Power 40 K		60 KW	80 KW	
cycle 1		Before	$9.3x10^{11}$	$3.5 \text{x} 10^{11}$	$5.6 \text{x} 10^{11}$	
	Up layer					
		After	$4.2x10^{11}$	1.1×10^{11}	$1.2 \text{x} 10^{11}$	
		Before	$9.8 \text{x} 10^{11}$	$7.4 \text{x} 10^{11}$	4.9×10^{11}	
	Down layer					
		After	3.6×10^{11}	$1.6 \text{x} 10^{11}$	$9.05x10^{10}$	
		Heating Power	40 KW	60 KW	80 KW	
cycle 3		Before	$8.9 \text{x} 10^{10}$	$7.1 \text{x} 10^{10}$		
	Up layer					
		After	$3.8 \text{x} 10^{10}$	$2.4 \text{x} 10^{10}$		
		Before	$3.3 \text{x} 10^{11}$	$5.7 \text{x} 10^{11}$	$2.7 \text{x} 10^{11}$	
	Down layer					
		After	$1.1 \text{x} 10^{11}$	$1.7 \text{x} 10^{11}$	5.1×10^{10}	
		Heating Power	40 KW	60 KW	80 KW	
cycle 5		Before	$1.3 \text{x} 10^{12}$	$1,4x10^{12}$	$1,09x10^{12}$	
	Up layer					
		After	$6.6 \mathrm{x} 10^{11}$	3.8×10^{11}	$1,9x10^{11}$	
		Before	$5.5 \text{x} 10^{11}$	$9,05x10^{11}$	$1x10^{12}$	
	Down layer					
		After	$1.5 \text{x} 10^{11}$	$2,4x10^{11}$	$1,6x10^{11}$	

Table 1: Area under the spectrum curve for two layers of PMSE Corresponding with three heating powers .

ratio of decrease in the area under spectrum after Heater turn-on		40 kW	60 kW	80 kW
cycle 1	Up layer Down layer	0.45 0.36	0.31 0.21	0.21 0.18
cycle 3	Up layer Down layer	0.42 0.33	0.33 0.29	N/A 0.18
cycle 5	Up layer Down layer	0.5 0.27	0.27 0.26	0.19 0.16

Table 2: Summary of normalized area under the coherent spectrum curve for heating cycles 1, 3, and 5.

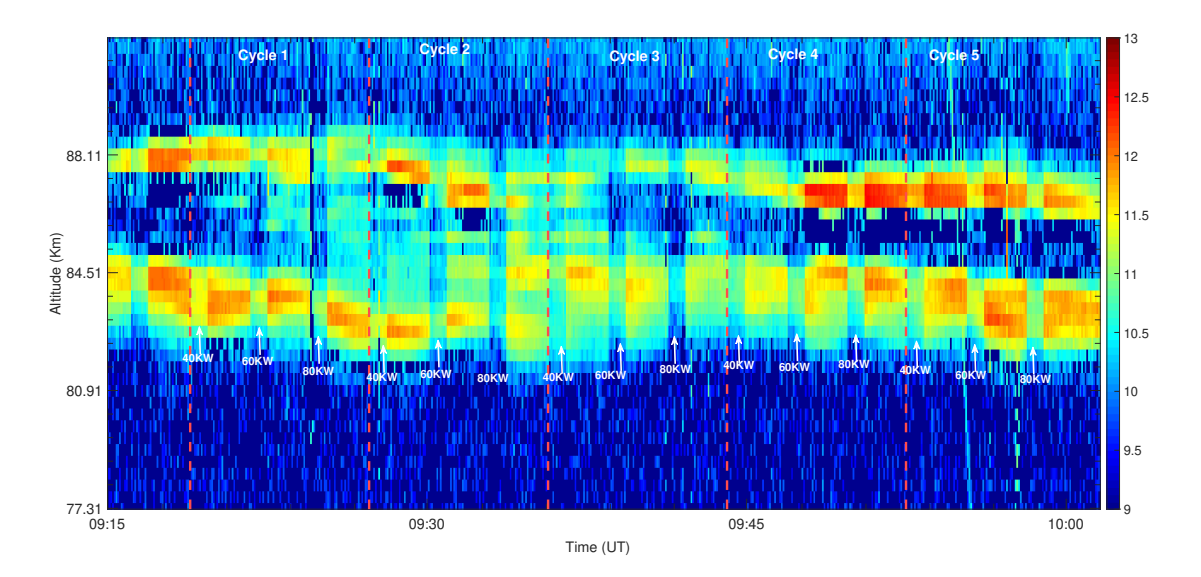


Figure 1: Time evolution of VHF PMSE during a modulated HF pump power heating experiment conducted at EISCAT on July 24, 2019. This experiment represents the first implementation of pump power stepping at a constant level during radio modulation of PMSE.

Heating cycle	Pump power	Up/Down layer	Min Amplitude during heating	Turn-off overshoot	Dust cloud parameters obtained from simulations
	40 kW	Up	0.5	N/A	$n_d/n_{e0} = 70\%$, $r_d = 5$ nm, $T_e/T_i = 1.6$, recomb = 0.1
	40 KW	Down	0.4	1.3	$n_d/n_{e0} = 80\%$, $r_d = 5$ nm, $T_e/T_i = 1.8$, recomb = 0.1
cycle 1	60 kW	Up	0.4	1.4	$n_d/n_{e0} = 70\%$, $r_d = 5$ nm, $T_e/T_i = 1.8$, recomb = 0.1
Cycle 1		Down	0.2	1.6	$n_d/n_{e0} = 80\%$, $r_d = 5$ nm, $T_e/T_i = 2$, recomb = 0.1
	80 kW	Up	N/A	N/A	N/A
		Down	0.2	1.9	$n_d/n_{e0} = 80\%$, $r_d = 5$ nm, $T_e/T_i = 2.2$, recomb = 0.1
	40 kW	Up	★ 0.5 (0.8)	2	$n_d/n_{e0} = 60\%$, $r_d = 5$ nm, $T_e/T_i = 1.8$, recomb = 0.2
		Down	0.4	1.4	$n_d/n_{e0} = 150\%$, $r_d = 3$ nm, $T_e/T_i = 2.25$, recomb = 0.1
cvcle 3	60 kW	Up	* 0.4 (0.55)	2.4	$n_d/n_{e0} = 60\%$, $r_d = 5$ nm, $T_e/T_i = 2$, recomb = 0.15
Cycle 3	00 K VV	Down	0.3	1.4	$n_d/n_{e0} = 150\%$, $r_d = 3$ nm, $T_e/T_i = 2.5$, recomb = 0.1
	80 kW	Up	0.3	1.6	$n_d/n_{e0} = 60\%$, $r_d = 5$ nm, $T_e/T_i = 2.2$, recomb = 0.1
	00 K VV	Down	0.2	~ 1	$n_d/n_{e0} = 150\%$, $r_d = 3$ nm, $T_e/T_i = 3$, recomb = 0.1
	40 kW	Up	0.5	2	$n_d/n_{e0} = 110\%$, $r_d = 3$ nm, $T_e/T_i = 3.2$, recomb = 0.1
	40 K W	Down	0.4	1.2	$n_d/n_{e0} = 150\%$, $r_d = 3$ nm, $T_e/T_i = 2.25$, recomb = 0.1
cvcle 5	60 kW	Up	0.3	~1.5	$n_d/n_{e0} = 110\%$, $r_d = 3$ nm, $T_e/T_i = 3.3$, recomb = 0.1
Cycle 5		Down	0.3	~1.5	$n_d/n_{e0} = 150\%$, $r_d = 3$ nm, $T_e/T_i = 2.5$, recomb = 0.1
	80 kW	$_{ m Up}$	0.2	1.1-1.2	$n_d/n_{e0} = 110\%$, $r_d = 3$ nm, $T_e/T_i \sim 3.4$, recomb = 0.1
	OUKW	Down	0.18	1.1-1.2	$n_d/n_{e0} = 150\%, r_d = 3 \text{ nm}, T_e/T_i \sim 3, \text{ recomb} = 0.1$

Table 3: Dust cloud parameters obtained from comparison of experiment and simulation for heating cycles $1,\,3,\,$ and 5 on July 24 .

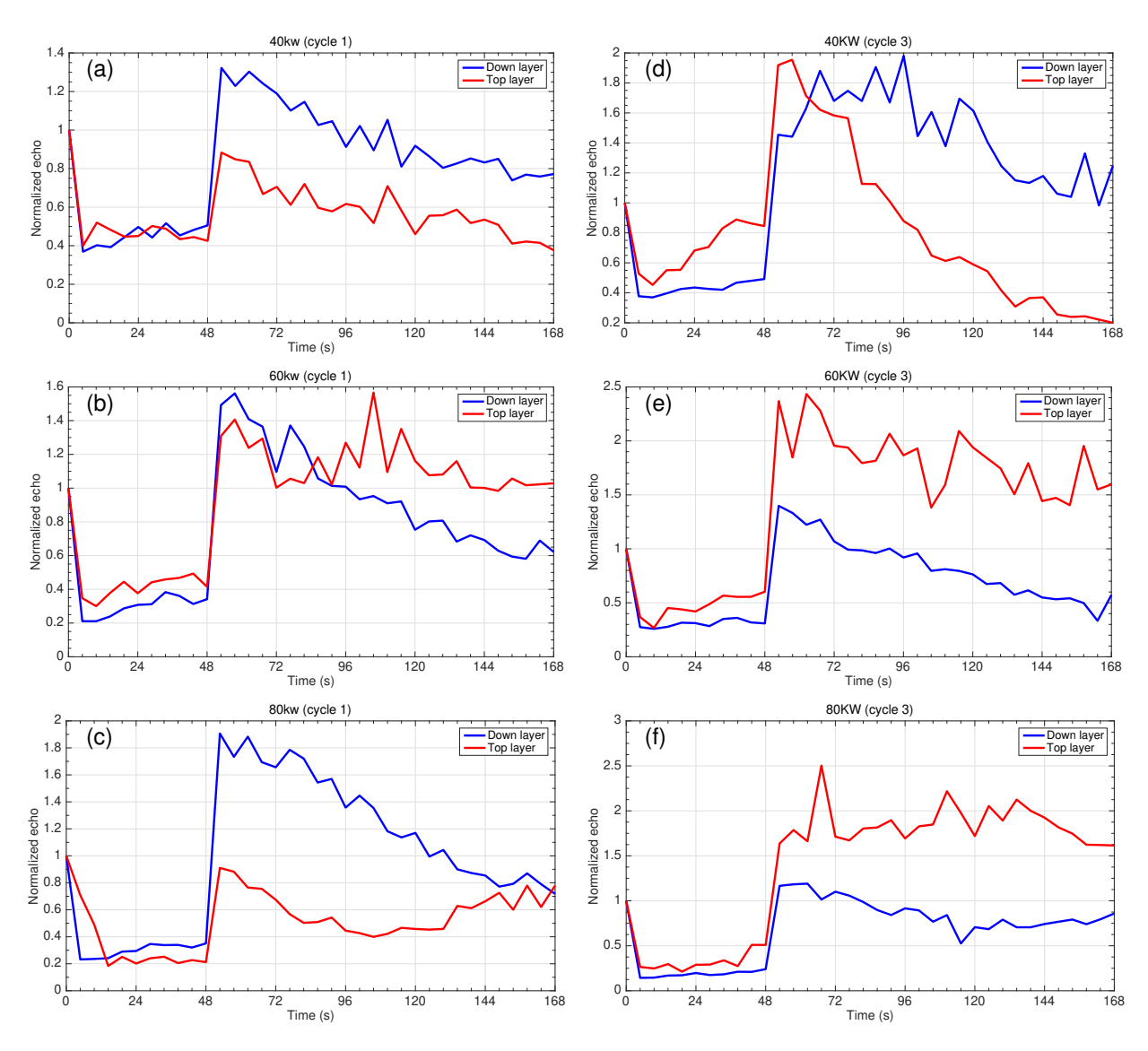


Figure 2: July 24, 2019. Normalized PMSE echo during heating experiment at EISCAT (48 sec heater on period and 120 sec heater off period). The modulated PMSE echo associated with heating cycle 1 (left column) and cycle 3 (right column) as shown Figure 1 is shown. The PMSE echo and modulated signal in the top and bottom layers are investigated separately.

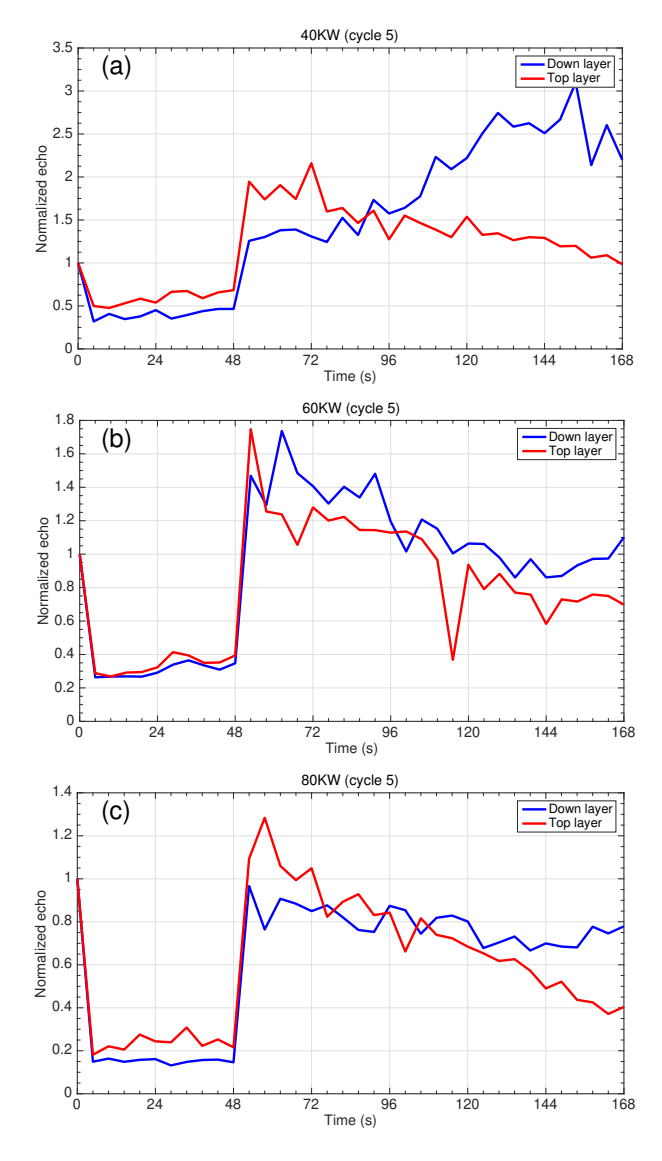


Figure 3: Normalized PMSE echo during heating experiment at EISCAT (48 sec heater on period and 120 sec heater off period) on July 24, 2019. The modulated PMSE echo associated with heating cycle 5 in Figure 1 is shown. The PMSE echo and modulated signal in the top and bottom layers are investigated separately.

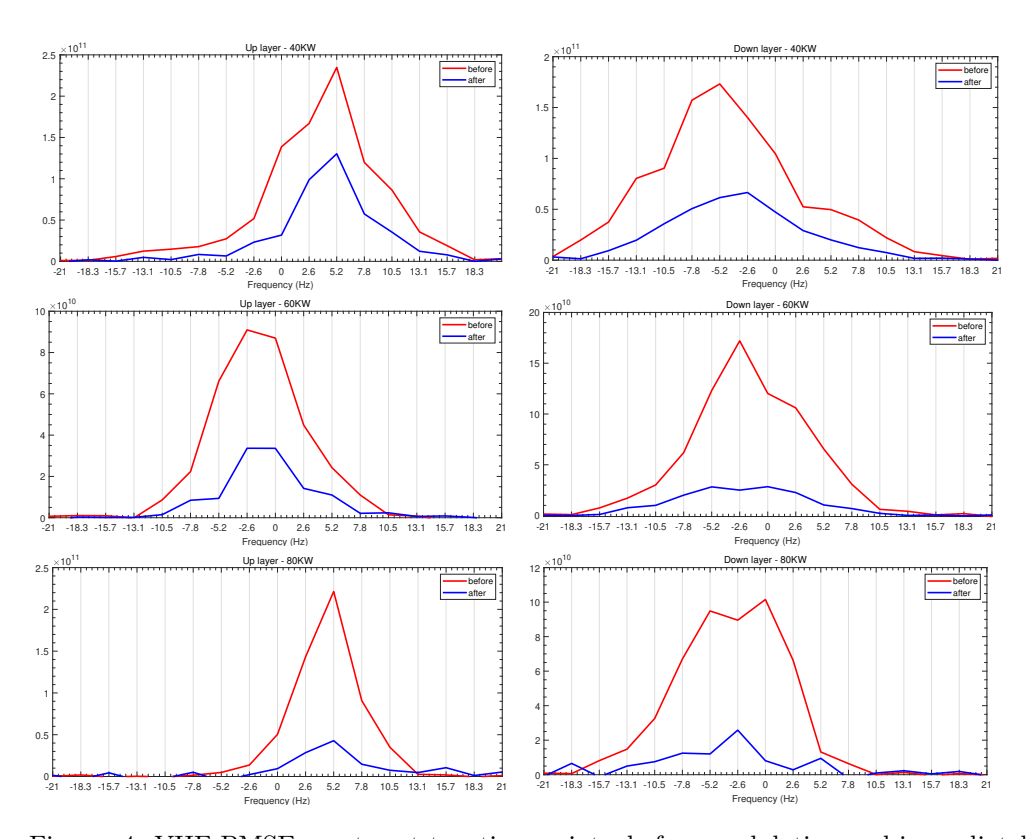


Figure 4: VHF PMSE spectra at two time points, before modulation and immediately after heating is turned on for both the upper (left panel) and lower (right panel) layers on July 24, 2019. Top, middle, and bottom panels correspond to $40~\rm kW,\,60~\rm kW,\,and\,80~\rm kW$ HF pump power, respectively.

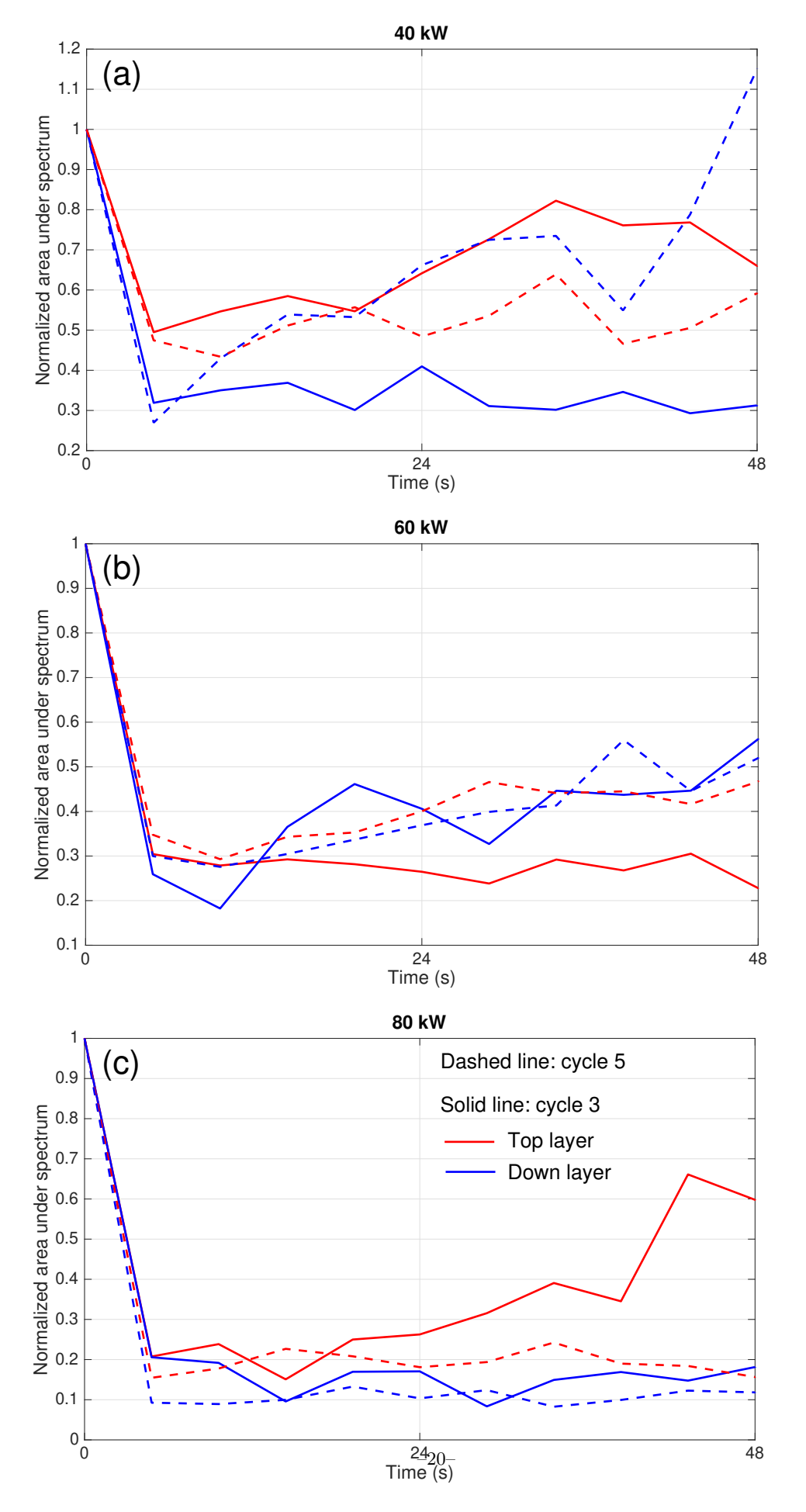


Figure 5: Corresponding normalized area under spectrum associated with two cycles 3 and 5 that are shown in Figure 2 and 3. The down layers are shown in blue and upper layers are shown in red.

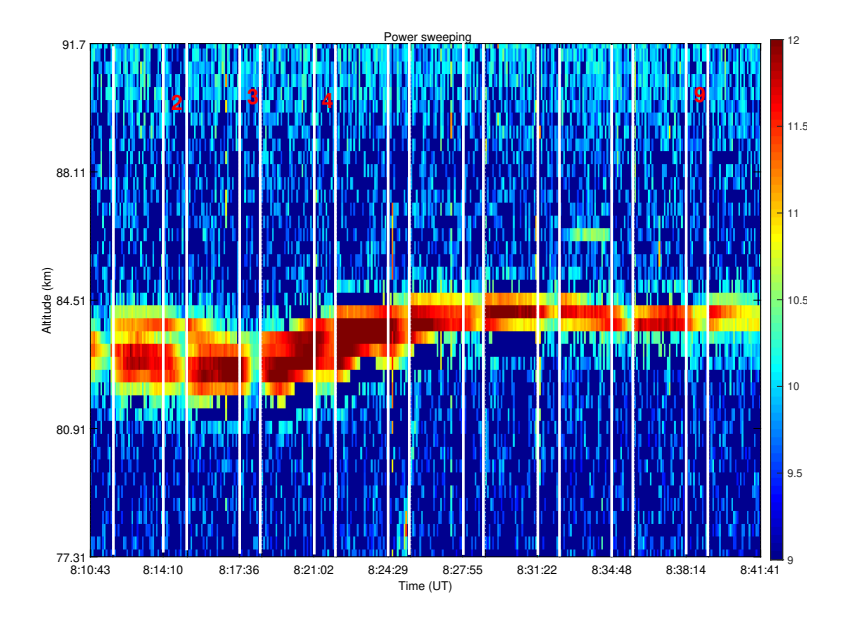


Figure 6: Time evolution of VHF PMSE during a modulated HF pump power heating experiment conducted at EISCAT on July 26, 2019. This experiment represents the first implementation of pump power sweeping during radio modulation of PMSE. The heating cycle is 62.4 sec.

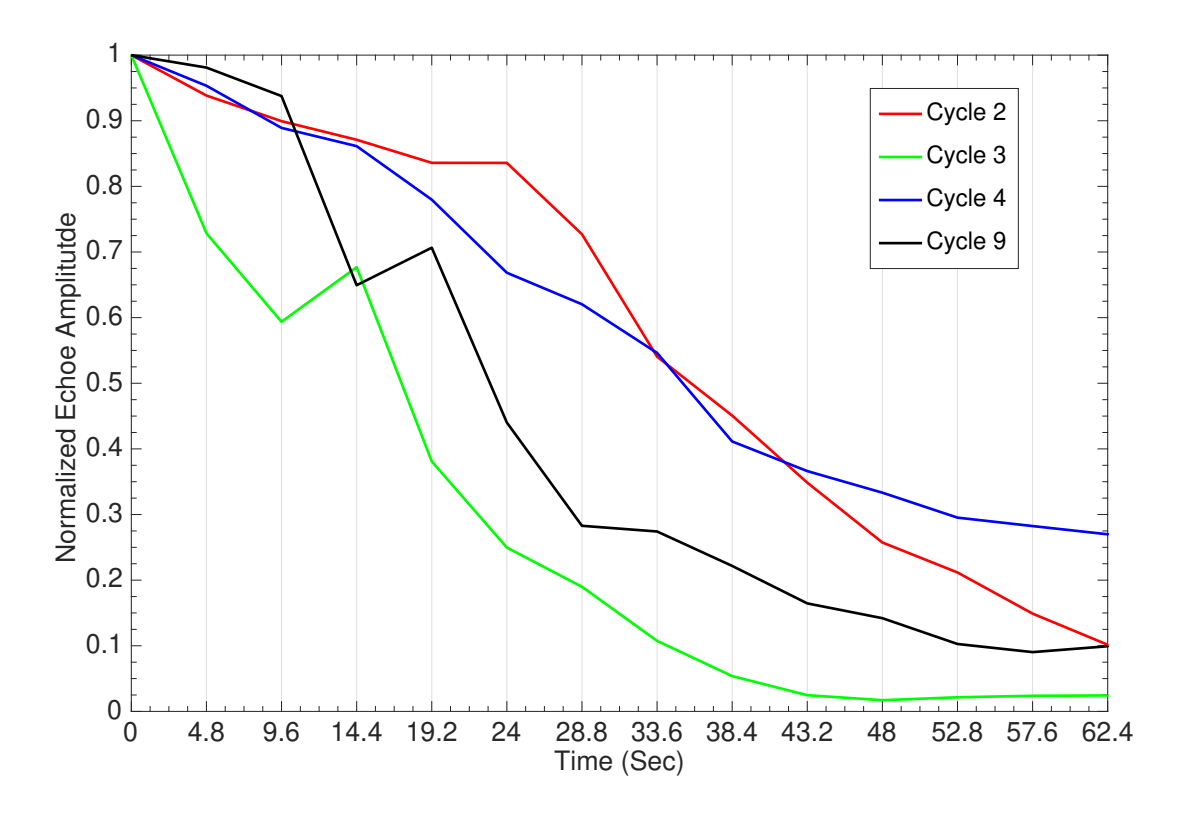


Figure 7: Normalized PMSE echo during heating experiment at EISCAT on July 26, 2019. The HF pump power gradually ramped up from zero to full power over the 62.4 sec.

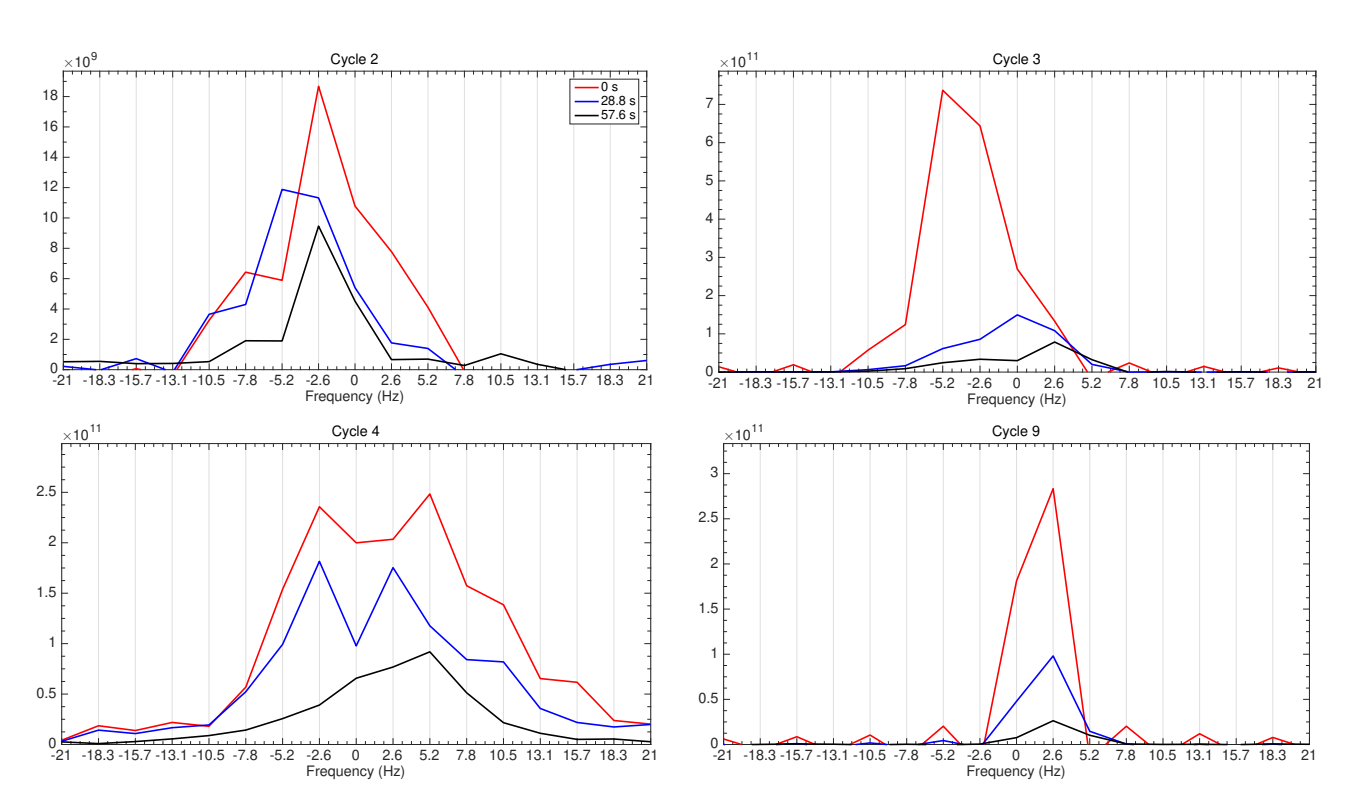


Figure 8: The spectra for the four selected cycles on July 26, 2019 are shown at three time points: 0 sec (before heating), 28.8 sec, and 57.6 sec, represented by red, blue, and black lines, respectively

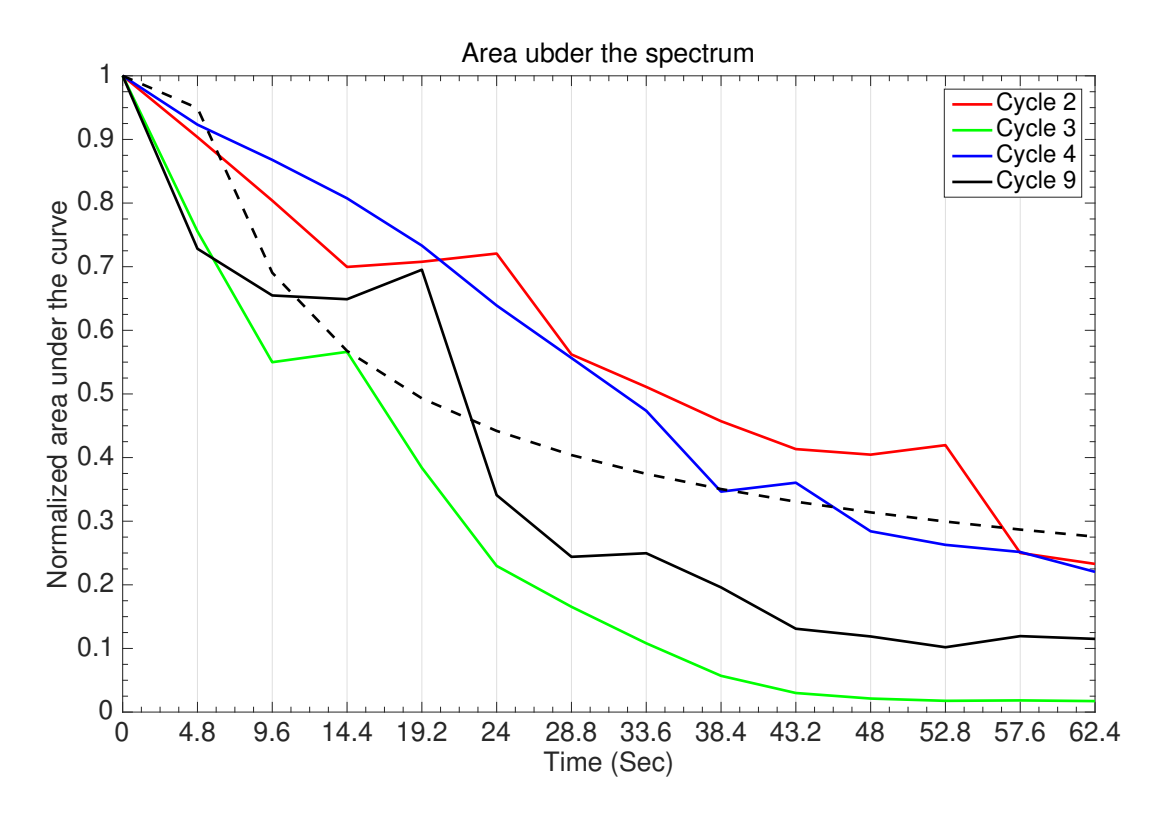


Figure 9: Normalized area under the spectral curve over a 62.4-sec interval for 4 selected heating cycles on July 26, 2019. The dashed line corresponds to $\tau_{\rm diff}/\tau_{\rm chg}$ obtained from Equations 1 and 2 with varying T_e/T_i during heating. The temperature increments are employed in 4.8 sec steps.

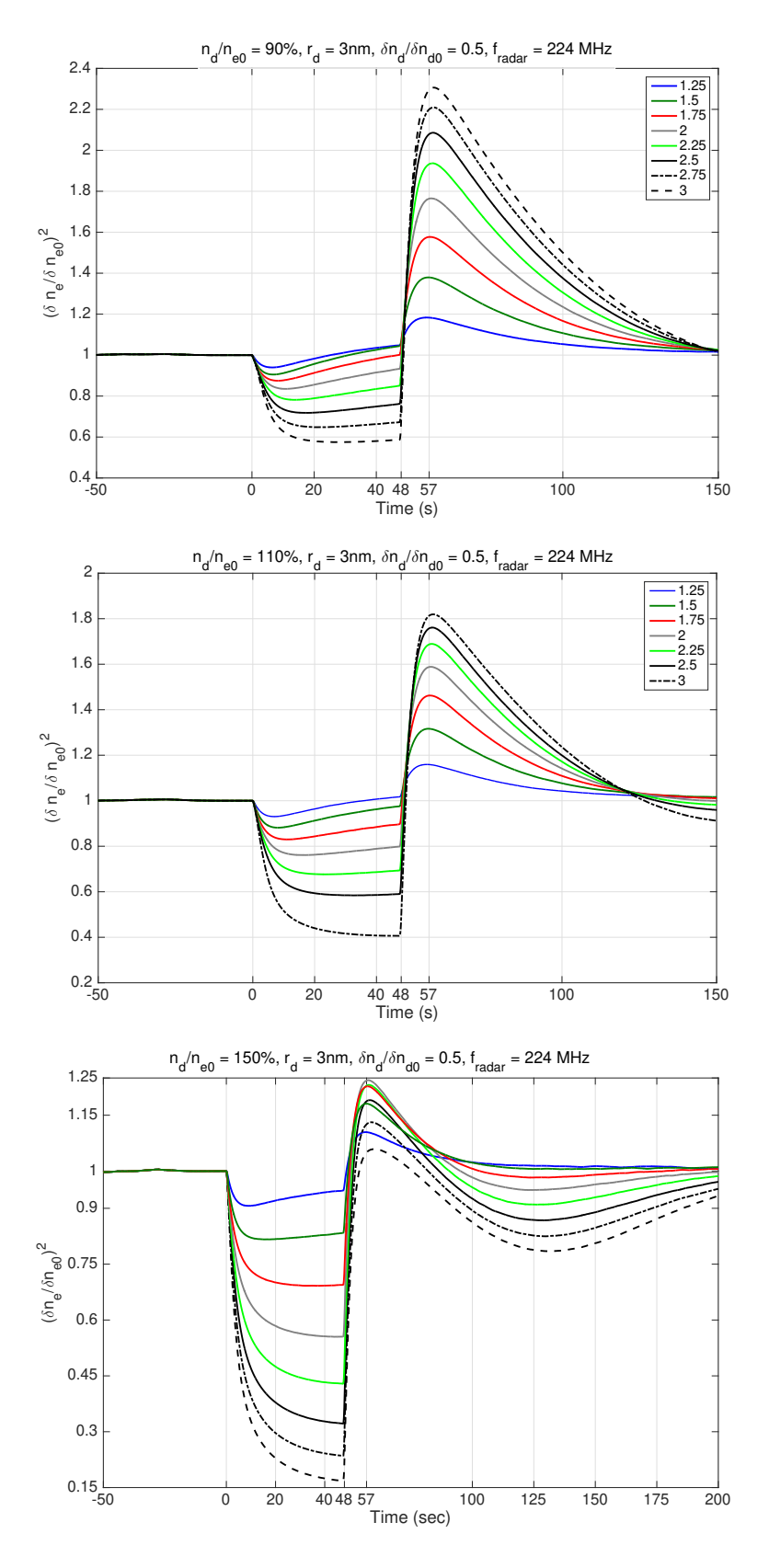


Figure 10: Simulation results for a dust radius (r_d) of 3 nm. Panels (a)–(c) show the effect of varying background dust density relative to electron density (n_d/n_{e0}) at 90%, 110%, and 150%, respectively. The recombination rate is fixed at 0.1, and the heating ratio (T_e/T_i) varies from 1.25 to 3. A radar frequency of 224 MHz and a dust density fluctuation amplitude of $\delta n_d/\delta n_{d0}=0.5$ are used. The color and line style representing each T_e/T_i value are consistent across all panels.

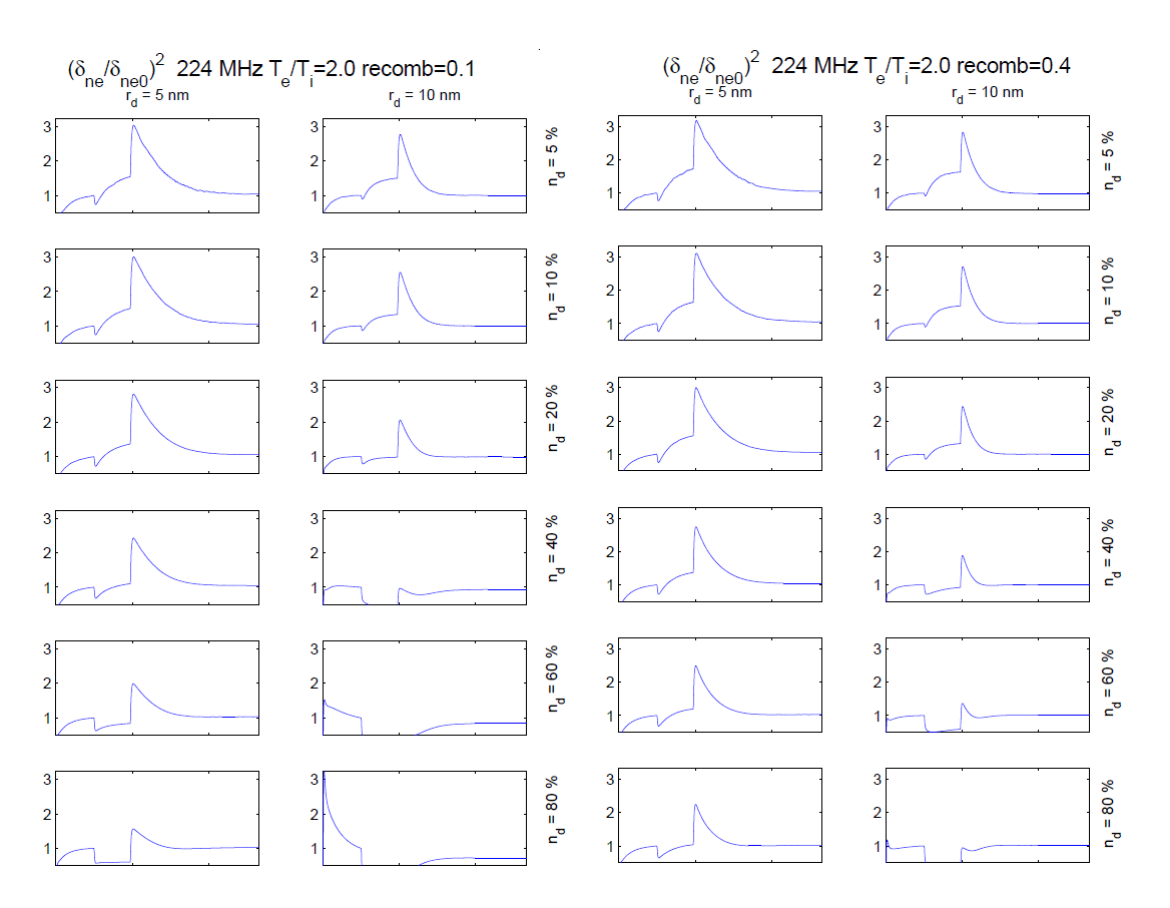


Figure 11: Numerical results for larger dust radii of 5 nm and 10 nm. Simulations consider dust densities of 20%, 40%, 60%, and 80% relative to the initial electron density (n_d/n_{e0}) , with a fixed heating ratio (T_e/T_i) of 2. The left panel shows results with a baseline recombination rate, while the right panel presents corresponding results with the recombination rate enhanced by a factor of 4.